Earth and Planetary Science Letters 444 (2016) 75–87

Contents lists available at ScienceDirect

Earth and Planetary Science Letters

www.elsevier.com/locate/epsl

Late Miocene–Pliocene Asian monsoon intensification linked to Antarctic ice-sheet growth

Hong Ao [a,*], Andrew P. Roberts [b], Mark J. Dekkers [c], Xiaodong Liu [a], Eelco J. Rohling [b,d], Zhengguo Shi [a], Zhisheng An [a], Xiang Zhao [b]

[a] State Key Laboratory of Loess and Quaternary Geology, Institute of Earth Environment, Chinese Academy of Sciences, Xi'an 710061, China
[b] Research School of Earth Sciences, The Australian National University, Canberra 2601, Australia
[c] Paleomagnetic Laboratory 'Fort Hoofddijk', Department of Earth Sciences, Faculty of Geosciences, Utrecht University, Budapestlaan 17, 3584 CD Utrecht, The Netherlands
[d] Ocean and Earth Science, University of Southampton, National Oceanography Centre, Southampton SO14 3ZH, UK

ARTICLE INFO

Article history:
Received 10 August 2015
Received in revised form 10 March 2016
Accepted 13 March 2016
Available online 8 April 2016
Editor: B. Buffett

Keywords:
environmental magnetism
East Asian monsoon
Chinese Loess Plateau
Red Clay
Late Miocene–Pliocene
Antarctic glaciation

ABSTRACT

Environmental conditions in one of Earth's most densely populated regions, East Asia, are dominated by the monsoon. While Quaternary monsoon variability is reasonably well understood, pre-Quaternary monsoon variability and dynamics remain enigmatic. In particular, little is known about potential relationships between northern hemispheric monsoon response and major Cenozoic changes in Antarctic ice cover. Here we document long-term East Asian summer monsoon (EASM) intensification through the Late Miocene–Pliocene (~8.2 to 2.6 Ma), and attribute this to progressive Antarctic glaciation. Our new high-resolution magnetic records of long-term EASM intensification come from the Late Miocene–Pliocene Red Clay sequence on the Chinese Loess Plateau; we identify underlying mechanisms using a numerical climate-model simulation of EASM response to an idealized stepwise increase in Antarctic ice volume. We infer that progressive Antarctic glaciation caused intensification of the cross-equatorial pressure gradient between an atmospheric high-pressure cell over Australia and a low-pressure cell over mid-latitude East Asia, as well as intensification of the cross-equatorial sea-surface temperature (SST) gradient. These combined atmospheric and oceanic adjustments led to EASM intensification. Our findings offer a new and more global perspective on the controls behind long-term Asian monsoon evolution.

1. Introduction

The Asian monsoon represents a major component of the global climate system and influences societal and economic activity for roughly half the world's population (Webster et al., 1998; Clift and Plumb, 2008). Uncovering past monsoon variability and dynamics is an important and challenging topic in paleoclimatic studies. The eolian Quaternary loess–paleosol and underlying Miocene–Pliocene Red Clay sequences on the Chinese Loess Plateau cover an area of ~300,000 km^2 and form deposits up to as thick as ~600 m (Liu, 1985; Qiang et al., 2011). These late Cenozoic eolian sequences contain a remarkable continental record of past Asian monsoon changes, which reflect dust transportation from arid central Asia to the semi-arid Loess Plateau, principally by the Asian winter monsoon (An et al., 1990, 2001; Guo et al., 2002). Over the past two decades, extensive studies of the loess–paleosol sequences have established the Quaternary record of Asian Monsoon variability at orbital-to-millennial time scales (Liu and Ding, 1998; An, 2014; An et al., 2015). The monsoon is suggested to be linked dynamically to changes in external forcing, i.e. solar insolation, and internal forcing, i.e. changing boundary conditions such as ice volume and ocean–atmosphere energy exchange (An et al., 1991, 2015; Ding et al., 1995; Liu and Ding, 1998; An, 2000; Sun et al., 2015; Yang et al., 2015). However, the Miocene–Pliocene evolution and driving mechanisms of the Asian Monsoon encoded in the underlying Red Clay sequence are still not well understood.

Within natural systems, magnetic mineral variations can reflect environmental changes, and can be quantified with magnetic techniques (Oldfield, 1991; Evans and Heller, 2003; Liu et al., 2012). Hence, mineral magnetic techniques have proven to be powerful tools for investigating paleoclimate history as encoded in iron-bearing minerals (Oldfield, 1991; Verosub and Roberts, 1995; Evans and Heller, 2003; Liu et al., 2012). Since Heller and Liu (1984, 1986) first recognized that the magnetic susceptibility variations in Chinese loess–paleosol sequences correlate with marine

* Corresponding author. Tel.: +86 29 62336218. Address: No. 97 Yanxiang Road, Xi'an 710061, Shaanxi, China.
E-mail address: aohong@ieecas.cn (H. Ao).

http://dx.doi.org/10.1016/j.epsl.2016.03.028
0012-821X/

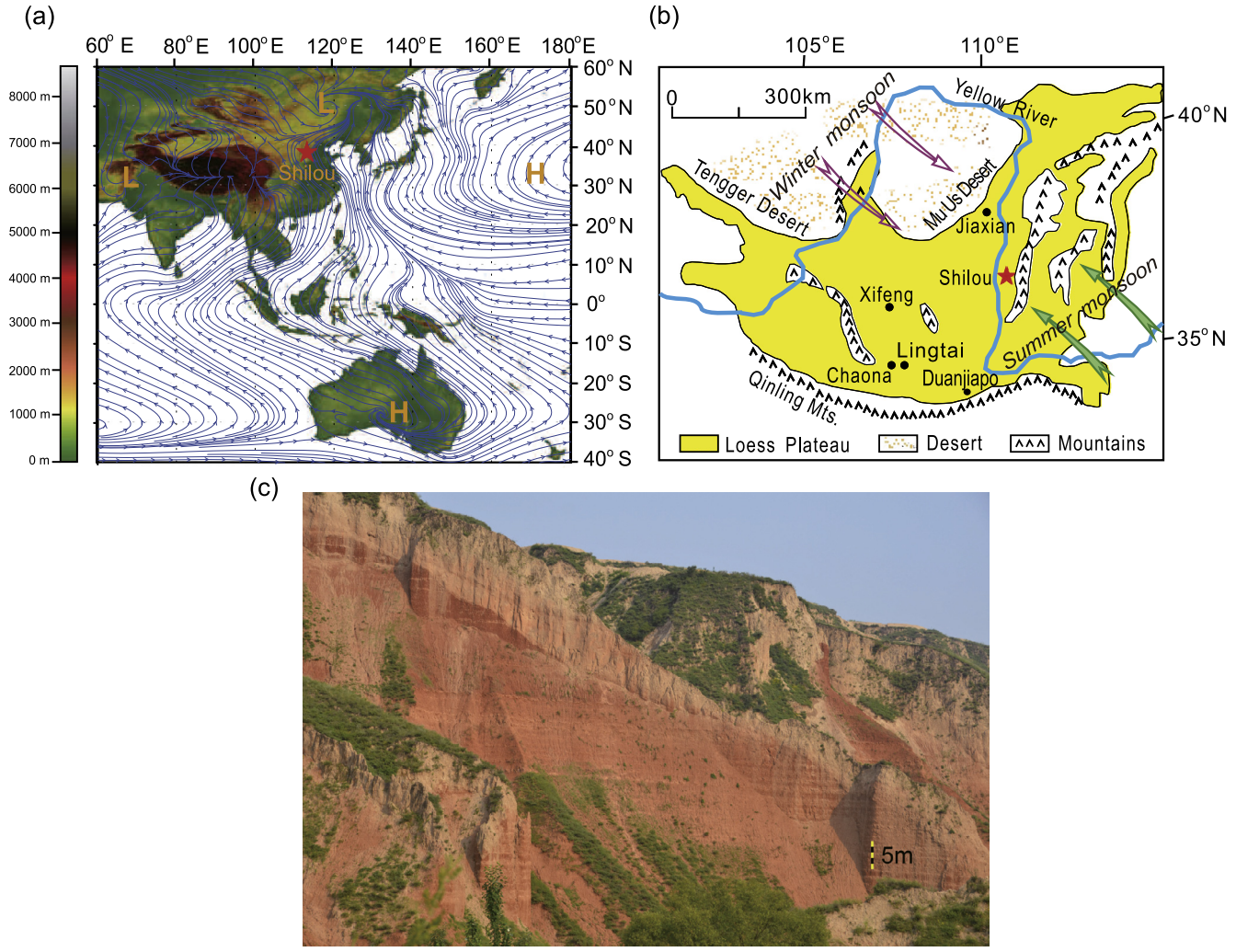

Fig. 1. Site location and atmospheric circulation. (a) Asian summer monsoon circulation from the surficial streamline field averaged from June to August for 1981–2010 based on the European Centre for Medium-Range Weather Forecasts (ECMWF) Reanalysis (ERA) data (Dee et al., 2011). ERA is the latest global atmospheric reanalysis produced by the ECMWF. The capitals 'H' and 'L' denote the locations of the pertinent high and low atmospheric pressure systems. (b) Map of the Chinese Loess Plateau with locations of the studied Shilou and other Red Clay sections mentioned in the text. (c) Photograph of the Shilou Red Clay sequence with alternating light red to reddish-yellow loess and reddish to brownish-red soil layers. Toward the top of the section the paleosols become more prominent with redder color, consistent with enhanced pedogenesis and summer monsoon intensity.

oxygen isotope records, numerous environmental magnetic studies have been conducted to better understand Quaternary paleoclimatic and paleoenvironmental changes (cf. Heller and Evans, 1995; Evans and Heller, 2001; Liu et al., 2007, 2015). More recently, environmental magnetism has been used to decipher pre-Quaternary paleoclimate history from the underlying Red Clay sequences (e.g., Liu et al., 2003; Hao et al., 2008; Nie et al., 2008a, 2010, 2014).

In contrast to northern hemisphere cooling that would weaken the Asian summer monsoon (Prell and Kutzbach, 1992; deMenocal and Rind, 1993; Chiang and Friedman, 2012), southern hemisphere cooling tends to enhance the Asian summer monsoon as indicated by modern observations (Xue et al., 2003), climate simulations (He et al., 1991) and Quaternary paleoclimate records (Rohling et al., 2009; An et al., 2011). Development of late Cenozoic Antarctic glaciation produced important global changes that had prominent influence on global climate (Zachos et al., 2001). However, little is known about its impact on contemporaneous Asian monsoon variability.

Here we reconstruct a pre-Quaternary history of the East Asian summer monsoon (EASM) from a mineral magnetic record of the Shilou Red Clay from the eastern Chinese Loess Plateau. We observe a long-term trend with EASM intensification from ~8 to 2.6 Ma. Using a numerical simulation of EASM response to an idealized stepwise increase in Antarctic ice volume, together with a marine oxygen isotopic record that documents Antarctic ice sheet expansion, we test for linkage between Antarctic glacial history and EASM intensification during the Late Miocene–Pliocene.

2. General setting

The present-day EASM season usually begins in late May–early June, when insolation change causes a temperature gradient between low pressures over mid-latitude Asia and high pressures over the western Pacific Ocean and Australia (Webster et al., 1998; Wang, 2006) (Fig. 1a). The EASM then transports heat and moisture from tropical oceans to continental Asia, such as to the Chinese Loess Plateau. The Shilou Red Clay sequence investigated here (36°55′N, 110°56′E) is situated on the eastern Chinese Loess Plateau, ~13 km southeast of Shilou city (Shanxi Province) and ~50 km east of the Yellow River (Fig. 1b). This region has a mean annual temperature of 9.2 °C and precipitation of 401 mm over the past 50 yrs.

The horizontally stratified Shilou Red Clay (Fig. 1c) is capped by Quaternary loess and is underlain by gray Triassic sandstone.

The Red Clay sequence, the focus of present study, consists of alternating light red to reddish-yellow loess deposits and reddish to brownish-red paleosols (Fig. 1c), where the latter formed during warm/humid periods (An et al., 2001). Since the thick continuous Red Clay is devoid of suitable material for radioisotopic dating, magnetostratigraphy is the most suitable tool for developing a robust age model. An existing magnetochronology for the Late Miocene–Pliocene Shilou Red Clay sequence (Xu et al., 2009) contains some ambiguous polarity divisions, which precludes unequivocal correlation to the geomagnetic polarity time scale (GPTS). The resulting age model is, therefore, ambiguous, which leads to imprecise interpretations when the reconstructed paleoclimate record is compared with other, well-dated, regional and global paleoclimate records. In order to establish a Late Miocene–Pliocene EASM record with a well-constrained age model, we sampled a new Red Clay succession at Shilou. The new section is located ~1 km west of the earlier investigated section which is ~70-m thick (Xu et al., 2009), at a location with a thicker natural outcrop of Red Clay (84.2 m thick).

3. Sampling and methods

To further extend our EASM record in this Red Clay sequence, we dug a well down to a stratigraphic level of 89.8 m (0 m stratigraphic level indicates the top of the section) to the contact with the underlying Triassic sandstone, in addition to the 84.2 m thick outcrop. We sampled the entire succession at 5–10-cm stratigraphic intervals for magnetostratigraphy and at ~2-cm intervals for EASM reconstruction. In order to obtain samples that were as fresh as possible, weathered surfaces were removed from the outcrop. A total of 1518 block samples were collected for magnetostratigraphy, which were oriented in the field using a compass. Two cubic (2 cm × 2 cm × 2 cm) samples were obtained from each of the 1518 oriented blocks for thermal demagnetization treatment to establish a magnetochronology. Leftovers of all oriented samples were kept in plastic bags, some of which were selected for mineral magnetic measurements, including temperature-dependent susceptibility (χ–T), acquisition curves of the isothermal remanent magnetization (IRM) and first-order reversal curve (FORC) measurements. A total of 4217 unoriented samples were collected for measurements of monsoon proxies, including low-frequency magnetic susceptibility (χ_{lf}), frequency-dependent magnetic susceptibility (χ_{fd}) and susceptibility of the anhysteretic remanent magnetization (χ_{ARM}).

Stepwise thermal demagnetization of the natural remanent magnetization (NRM) was conducted using an ASC TD-48 thermal demagnetizer. Samples were stepwise heated at 20–50 °C increments to a maximum temperature of 585 °C (13 demagnetization steps). More than 90% of the initial NRM was demagnetized at 585 °C, above which paleomagnetic directions became erratic, which precludes directional interpretation. After each demagnetization step, the NRM was measured with a 3-axis 2-G Enterprises Model 755-R cryogenic magnetometer housed in a magnetically shielded space at the Institute of Earth Environment, Chinese Academy of Sciences (Xi'an, China). Demagnetization results were evaluated using orthogonal vector component diagrams (Zijderveld, 1967); the characteristic remanent magnetization (ChRM) direction for each sample was computed using least-squares fitting (Kirschvink, 1980). Principal component analysis (PCA) was performed using the PaleoMag software (Jones, 2002); least-squares fits were anchored to the origin of the orthogonal diagrams. Not all collected samples were subjected to paleomagnetic measurements. Samples were first measured at 20-cm stratigraphic intervals. If polarity divisions were not clearly suggested in some intervals, additional stratigraphic levels were measured at 10-cm and even 5-cm sampling intervals until a detailed and unambiguous polarity stratigraphy resulted. Thus, 978 stratigraphic levels were subjected to paleomagnetic analysis to establish a magnetochronology for the Shilou Red Clay sequence.

Temperature-dependent susceptibility curves were measured in an argon atmosphere from room temperature to 700 °C and back to room temperature using a MFK1-FA susceptometer equipped with a CS-3 high-temperature furnace (AGICO, Brno, Czech Republic). IRM acquisition curves were determined using an ASC IM-10-30 pulse magnetizer with stepwise increasing fields applied to a maximum field of 2.7 T. Remanence measurements were made with an AGICO JR-6A spinner magnetometer. IRM acquisition curves were measured with 34 field steps. FORC measurements (Roberts et al., 2000, 2014) were made using the variable resolution FORC protocol (Zhao et al., 2015) with a Princeton Measurements Corporation (Model 3900) vibrating sample magnetometer (VSM). For each sample, 80 FORCs were measured with fields up to ~300 mT, an averaging time of 200 ms and a smallest field increment of 1 mT. Data were processed using the software of Zhao et al. (2015) with a smoothing factor of 2.

All 4217 unoriented samples were powdered and were then packed into non-magnetic cubic boxes (2 cm × 2 cm × 2 cm) for χ_{lf}, χ_{fd} and χ_{ARM} measurements. χ_{lf} was measured with a Bartington Instruments MS2 magnetic susceptibility meter at 470 Hz. High-frequency magnetic susceptibility (χ_{hf}) was measured at 4700 Hz to calculate the summer monsoon proxy χ_{fd} ($\chi_{fd} = \chi_{lf} - \chi_{hf}$). ARM was imparted using a peak alternating field (AF) of 100 mT and a 0.05 mT direct current (DC) bias field, and was measured using a 2-G Enterprises Model 755-R cryogenic magnetometer. χ_{ARM} was obtained by dividing the mass-normalized ARM intensity by the DC field strength (expressed in units of H, i.e., A/m). In addition, a stacked EASM record was established based on χ_{lf} proxy data from the Shilou, Chaona (Nie et al., 2007), Xifeng (Sun et al., 1998a), Duanjiapo (An et al., 2000) and Lingtai (Sun et al., 2010) Red Clay sections. Each χ_{lf} time series was first normalized (between 0 and 1) to give the same weighting to each record in the stack. Then each normalized record was interpolated linearly at 1-ka intervals. Finally, χ_{lf} data for each time interval were averaged to form a new time series (our stacked EASM record). The stacked EASM record improves the signal-to-noise ratio of the climate signal and provides a useful Late Miocene–Pliocene EASM reference curve.

Four numerical experiments were performed to evaluate EASM responses to an idealized stepwise growth of East and West Antarctic ice sheets. The National Center for Atmospheric Research (NCAR) Community Atmosphere Model version 3 (CAM3) (Collins et al., 2004) was used for this purpose. The Community Land Model version 3 (CLM3) is coupled to CAM3 to calculate land surface processes. In our four experiments (from scenarios S-1 to S-4), all boundary conditions were the same except for different Antarctic ice sheet distributions, with the aim of evaluating the sensitivity of EASM responses to remote Antarctic ice-sheet growth. Antarctic topography and other boundary conditions are set as present-day in each experiment. Modern monthly sea surface temperatures were chosen along with pre-industrial atmospheric greenhouse gas concentrations (CO_2 = 280 ppm, CH_4 = 760 ppb, N_2O = 270 ppb). Four Antarctic ice sheet configurations, from no ice sheet (scenario S-1) to modern ice sheet size (scenario S-4), were simulated based on progressive increases in ice sheet size from East to West Antarctica, which reflects their progressive Late Miocene–Pliocene growth (Zachos et al., 2001). Scenario S-2 refers to 33% of the total modern Antarctic ice sheet, with all ice located in the East (i.e., equal to a situation in which only present-day East Antarctica is covered with ice). Scenario S-2 represents the situation at 8–10 Ma (Zachos et al., 2001), the beginning of the time interval studied here. Scenario S-3 refers to 66% of the total modern Antarctic ice sheet located in East and central Antarc-

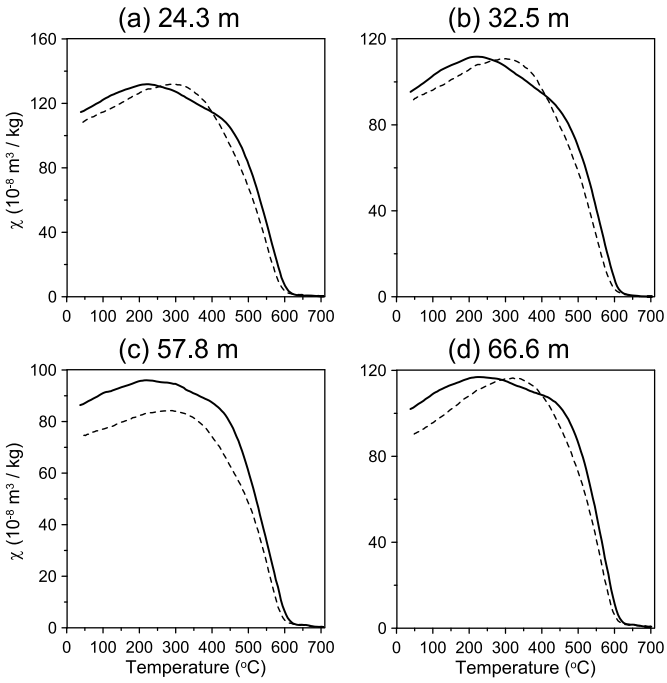

Fig. 2. χ–T curves for selected samples from the Shilou Red Clay sequence. The solid and dashed lines represent heating and cooling curves, respectively.

tica (i.e., equal to present-day ice coverage of East and central Antarctica), which is similar to the latest Miocene–earliest Pliocene situation (Zachos et al., 2001). Ice-sheet thickness variations are not considered in the simulations. Hence, our simulated climatic effect of Antarctic glaciation on monsoons is entirely produced by ice-induced albedo changes. All experiments were performed at a horizontal resolution of T42, which corresponds approximately to grid cells of 2.8° × 2.8°. After a spin-up time of 15 yrs, each experiment was integrated for another 15 yrs and the corresponding results were averaged. The response of the Australian high, Asian low, cross-equatorial pressure gradient, June–July–August (JJA) precipitation and JJA 850 hPa monsoon wind velocity are examined as the EASM response to four different Antarctic ice sheet distributions. Precipitation and wind speed are averaged for the EASM area (105–120°E and 20–40°N). The Australian high (120–150°E, 20–35°S) and Asian low-pressure cells (80–110°E, 25–40°N) are calculated from the atmospheric pressure at sea level averaged over the respective fixed areas. The cross-equatorial pressure gradient is calculated as the mean sea level pressure over the Australian high and Asian low-pressure cell regions. A larger pressure gradient gives rise to a stronger EASM. Our simulations are designed as a sensitivity experiment to examine physical processes and are not meant to exactly replicate Antarctic glacial history and boundary conditions during the Late Miocene–Pliocene.

4. Results

4.1. Magnetic mineralogy

All measured χ–T heating curves (Fig. 2) are characterized by a major χ decrease at 500–600 °C, which is consistent with the ubiquitous occurrence of magnetite in the Red Clay. The presence of hematite is usually masked magnetically by the much stronger magnetization of small amounts of magnetite, thus its expression on χ–T curves is generally subdued when both magnetite and hematite are present. Slight decreases up to 680 °C indicate a contribution from hematite. The almost reversible heating and cooling curves indicate minimal transformation of magnetic minerals during thermal treatment.

The behavior of magnetite and mixtures of hematite and goethite can be characterized more easily using IRM acquisition curve analysis (Fig. 3). The major IRM increase below 300 mT indicates a dominant contribution from magnetite to the magnetic mineralogy, whereas gradual increases to 2700 mT indicate that hematite and possibly goethite are also present (Fig. 3). Cumulative log-Gaussian decomposition analysis of IRM acquisition curves (Kruiver et al., 2001) indicates the presence of two magnetic mineral components: a low-coercivity component (magnetite) and a high-coercivity component (hematite/goethite) (Fig. 3 and Table S1). The low-coercivity component makes a higher contribution (>∼60%) to the acquired IRM than the high-coercivity component (Table S1). On a mass-specific basis, however, magnetite has a low-field IRM that is about two orders of magnitude stronger than hematite and goethite (Dunlop and Özdemir, 1997), so that large hematite and goethite concentrations are necessary to contribute substantially to the remanence when magnetite is also present.

All FORC diagrams contain a central ridge with maximum contour density at a B_c value of ∼10 mT (Fig. 4), which indicates the presence of noninteracting single domain (SD) magnetite (Roberts et al., 2000, 2014; Egli et al., 2010). Substantial superparamagnetic (SP) components also exist in the samples as suggested by a secondary peak near the origin of the plot as well as by a vertical distribution immediately adjacent to the B_u axis in the lower half plane (Roberts et al., 2000, 2014; Pike et al., 2001). The divergent pattern of the outer contours along the B_u axis points to a small pseudo-single-domain (PSD) component (Roberts et al., 2000, 2014; Muxworthy and Dunlop, 2002). Thus, the FORC distributions reveal a fine-grained magnetite population with a rather broad size distribution from SP/SD to the small PSD size range in the Red Clay.

4.2. Magnetochronology

Detailed paleomagnetic analysis served to formulate a robust age model for the Shilou section. After removal of a low-temperature secondary overprint at 150–200 °C, the characteristic remanent magnetization (ChRM) unblocked during demagnetization up to 585 °C (Fig. 5). This demagnetization behavior indicates that magnetite is the dominant ChRM carrier, which is consistent with previous paleomagnetic studies of Late Miocene–Pliocene Red Clay on the Chinese Loess Plateau (Sun et al., 1997, 1998a, 1998b; Qiang et al., 2001). In general, the ChRM is represented by a relatively straightforward unidirectional trajectory toward the origin of orthogonal vector demagnetization plots from 200 to 585 °C (Fig. 5). From the 978 demagnetized levels, 739 (76%) yielded reliable ChRM components (Table S2) based on strict selection criteria. Data from at least 4 (but typically 7–10) consecutive demagnetization steps above 200 °C were used to determine the ChRM direction, with a maximum angular deviation (MAD) of <10° (but typically 4–7°) for the respective line fits. Virtual geomagnetic pole (VGP) latitudes calculated from the 739 ChRM directions are used to establish the Shilou magnetostratigraphy (Fig. 6).

Biostratigraphic constraints from the micromammal *Meriones* sp. place the lower Shilou Red Clay in the Late Miocene (Xu et al., 2012), which enables unequivocal correlation of the magnetostratigraphy to the geomagnetic polarity timescale (GPTS) (Hilgen et al., 2012): the section appears to be continuous from the youngest portion of polarity chron C4r to subchron C2A.1n (Fig. 6). The base of the Shilou Red Clay falls just below the lower boundary of subchron C4n.2n, with an age of ∼8.2 Ma based on linear extrapolation of sedimentation rates within subchron C4n.2n. The average sedimentation rate of the whole Shilou Red Clay sequence is 15.5 m/Ma, while the older part has a higher sedimentation rate than the younger part (Fig. 7). There is a smooth and linear relationship between stratigraphic depth and magnetostratigraphic age, without abrupt shifts (Fig. 7), which indicates

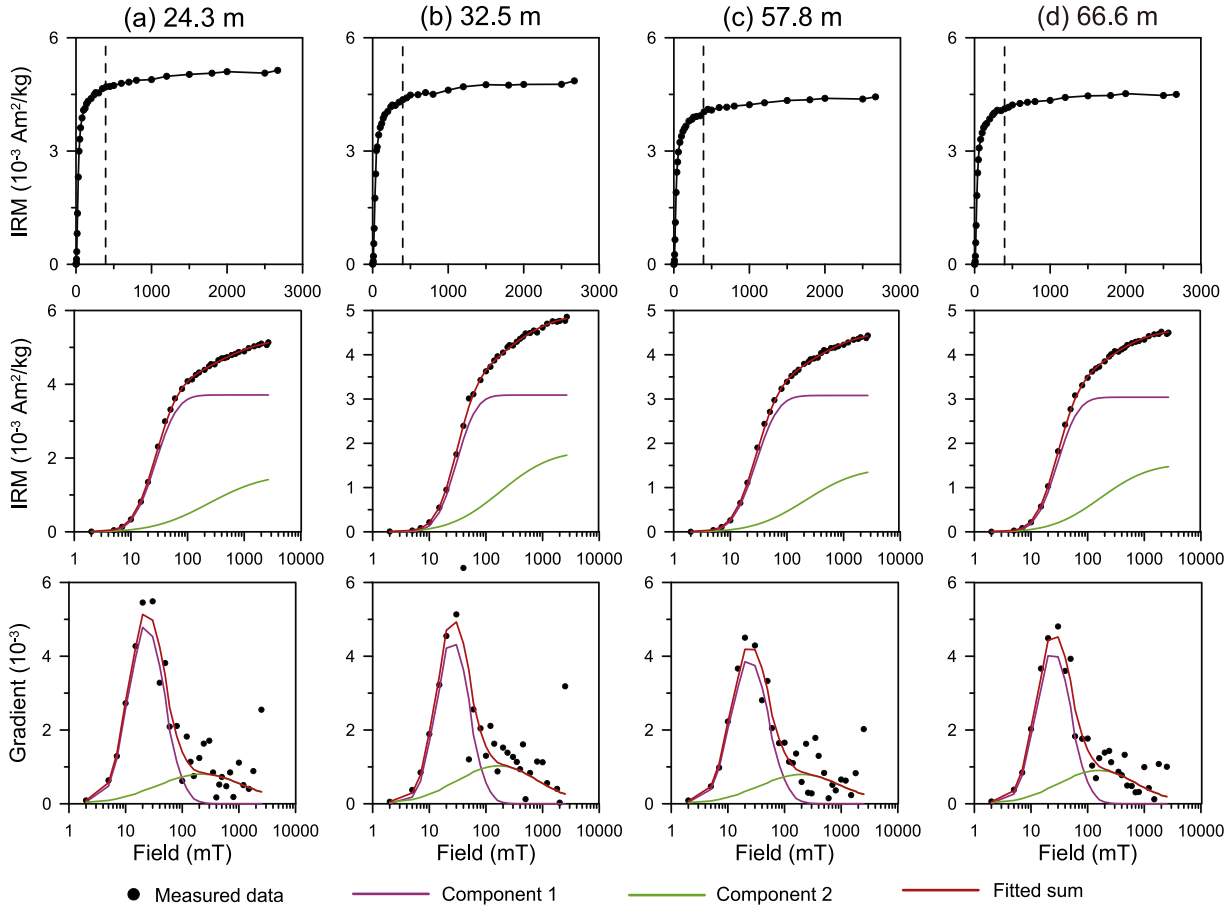

Fig. 3. Isothermal remanent magnetization (IRM) acquisition curves plotted with linear and logarithmic field axes, respectively, and gradient acquisition plots (according to the terminology of Kruiver et al. (2001)) for typical samples from the Shilou Red Clay sequence (the same samples as in Fig. 2). The dashed vertical lines at 300 mT are shown to aid distinction between low- and high-coercivity portions of the IRM acquisition curves.

relatively steady, continuous long-term sedimentation and a clear-cut magnetochronology. Therefore, an age model between 8.2 and 2.6 Ma for the Shilou Red Clay is established via linear interpolation using magnetic reversal boundaries as age control.

4.3. Late Miocene–Pliocene EASM variations

On the Loess Plateau, EASM precipitation – as a rule of thumb associated with elevated temperatures – drives pedogenesis and *in situ* formation of fine-grained magnetic minerals (An et al., 1990; Nie et al., 2008b). Also in the Shilou Red Clay, pedogenic fine-grained magnetite (ranging from SP/SD up to small PSD sizes, i.e., from <30 nm up to ~1000 nm) dominates the magnetic mineralogy (Figs. 2–4). Therefore, χ_{lf}, which is controlled by these fine-grained particles, has been shown to be a meaningful EASM proxy for Quaternary loess and the underlying Red Clay (An et al., 1990, 2001; Nie et al., 2008b; Sun et al., 2010). Furthermore, χ_{fd} and χ_{ARM} of the Red Clay are also useful EASM proxy parameters because they are sensitive to pedogenic SP and SD particle content variations (Hunt et al., 1995; Nie et al., 2008b, 2014). Greater EASM precipitation brings strengthened pedogenesis, which in turn leads to increased fine-grained pedogenic magnetite concentration and, thus, to high values of χ_{lf}, χ_{fd} and χ_{ARM}. Hence, we use all three parameters (χ_{lf}, χ_{fd} and χ_{ARM}) (Table S3), which vary coherently in the Shilou Red Clay, to construct a detailed proxy record of Late Miocene–Pliocene EASM intensity changes (Fig. 8). This proposition is supported by positive linear correlations among magnetic susceptibility data from Loess Plateau surface soils and modern mean annual precipitation (Maher and Thompson, 1995; Nie et al., 2014).

We observe a distinct upward increasing trend in χ_{lf}, χ_{fd} and χ_{ARM} values (Fig. 8a–c). A similar χ_{lf} trend is observed for other Red Clay sequences on the Chinese Loess Plateau, at Chaona (Nie et al., 2007), Xifeng (Sun et al., 1998a), Duanjiapo (An et al., 2000) and Lingtai (Sun et al., 2010) (Fig. 8d–g). The consistently increasing trends for Red Clay sequences indicate long-term strengthening of pedogenesis, linked to EASM intensification, from 8.2 to 2.6 Ma. Minor differences among the records probably imply that – superimposed on the underlying long-term trend – EASM influence was regionally variable across the Loess Plateau as it was during the Quaternary (Hao and Guo, 2005) or that there exist minor differences in sedimentary records (e.g., variable continuity) or in short-term age model construction. In order to better capture consistent long-term changes and to minimize regional differences and issues associated with short-term chronological alignments, we establish a stacked EASM record (Table S3) based on χ_{lf} proxy data from the Shilou, Chaona, Xifeng, Duanjiapo and Lingtai Red Clay sections (Fig. 8h), where higher values indicate higher EASM precipitation. The long-term monsoon intensification trend is clear in our stacked EASM record (Fig. 8h). In line with stronger pedogenesis and higher Pliocene monsoon precipitation, the upper part of the Shilou Red Clay has a redder color than the lower part (Fig. 1c), along with more Fe–Mn mottles, nodules, concretions, and coatings in soil profiles, whose formation is related to strong variations in soil moisture conditions (Roberts, 2015). Such indicators of soil redox changes indicate a much wetter soil environment than at present (Roberts, 2015). A long-term EASM increase from

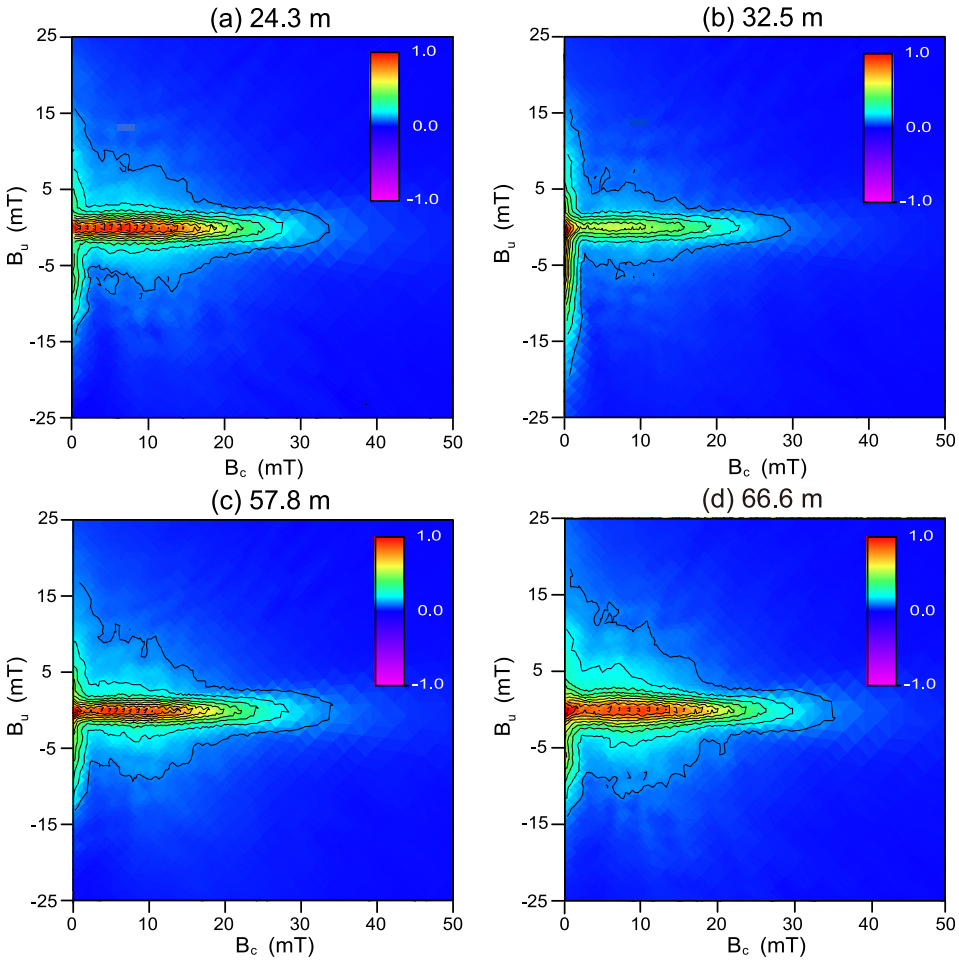

Fig. 4. FORC diagrams for selected samples from the Shilou Red Clay sequence (the same samples as in Figs. 2 and 3). The FORC diagrams are scaled to their respective maximum contour density.

~11 to 2.6 Ma is also inferred from hematite/goethite ratios at Ocean Drilling Program Site 1148 from the South China Sea (Clift, 2006) (Fig. 8i), with support from stable carbon isotope measurements of terrestrial black carbon in the same core (Jia et al., 2003).

4.4. Climate-model simulation

We use numerical simulations (Fig. 9) to evaluate the sensitivity of EASM responses to remote Antarctic ice-sheet growth and associated changes in Antarctic albedo. At times with limited Antarctic ice cover (scenario S-1, a case similar to the Mid-Miocene Climatic Optimum (Zachos et al., 2001)), the Australian high and Asian low are found to be weakly developed, with a reduced cross-equatorial pressure gradient between them (Fig. 9). This results in low surface wind speeds (2.23 m/s) and precipitation (2.8 mm/d) over the EASM area (105–120°E, 20–40°N). With increasing Antarctic ice cover, which is represented in an idealized manner as an East Antarctic ice cap with 33% of the total modern Antarctic ice volume (scenario S-2) or as ice cover in East and central Antarctica with 66% of the present ice volume (scenario S-3), the Australian high, Asian low, cross-equatorial pressure gradient, and EASM precipitation and velocities are all enhanced. For cases with completely developed Antarctic ice sheets (scenario S-4), a case similar to the Late Pliocene situation (Zachos et al., 2001), the Australian high, Asian low and cross-equatorial pressure gradient are further enhanced, which yields still higher EASM speed (3.05 m/s) and precipitation (3.7 mm/d). Overall, simulated EASM precipitation increases by 37% from scenarios S-1 to S-4. Spatially, stronger southerly or easterly winds that indicate an intensified monsoon are simulated over most East Asia for progressive Antarctic ice-sheet growth (Fig. S1). The easterly wind anomaly over southern China turns northward and becomes a southerly wind anomaly over northern China. An intensified summer monsoon transports more water vapor to Asia, which is associated with higher precipitation. The main difference between scenarios S-1 and S-2 is a moderate increase in summer precipitation over most of East Asia. From scenario S-2 to S-3, a significant precipitation increase occurs, especially in eastern China. When compared to scenario S-3, in scenario S-4 summer precipitation becomes heavier over northern China and lighter over southern China. Overall, our simulation results indicate that Antarctic ice sheet expansion enhances East Asian summer monsoon precipitation and winds despite spatial differences in the patterns of these changes.

5. Discussion

Our new detailed magnetostratigraphy considerably improves the polarity chron structure of the Shilou Red Clay, relative to previous work (Xu et al., 2009) (Fig. 10). The previous correlation of the Shilou magnetostratigraphy to the GPTS suggested an age range of 11–2.6 Ma (Xu et al., 2009), but with some polarity zones defined based on only one sample (Fig. 10). However, a single sample is insufficient for defining a polarity chron. If such equivocal data are not used to define polarity intervals, a re-interpretation of the previous magnetostratigraphy would lead to a similar result as our magnetostratigraphy (Fig. 10). Because of improved definition of

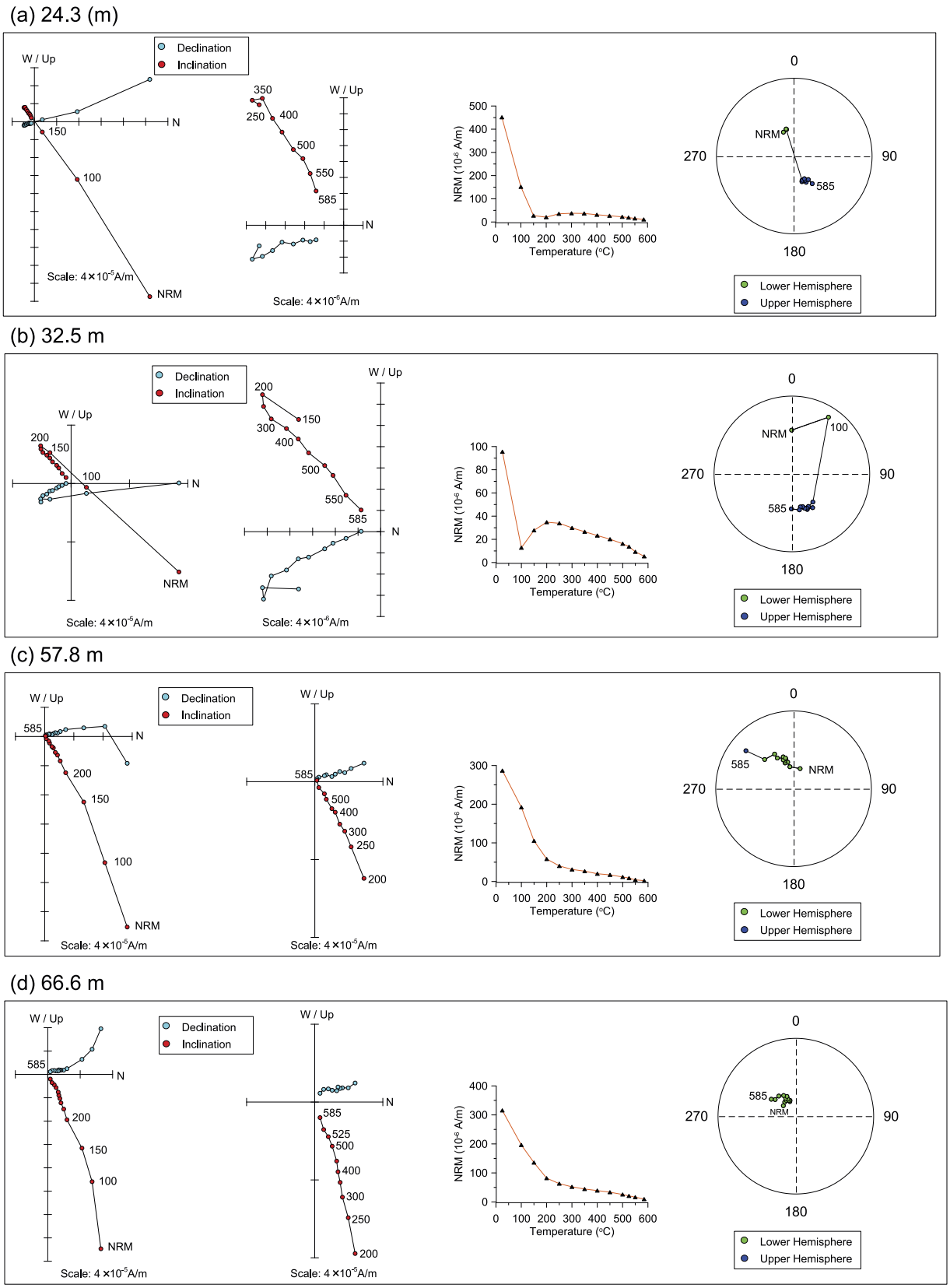

Fig. 5. Demagnetization diagrams for stepwise thermal demagnetization of the natural remanent magnetization (NRM) data (plots in the second column are magnifications of the left-most plots), their decay curves (plots in the third column), and corresponding equal-area stereographic projections (right-most plots) for selected samples from the Shilou Red Clay (the same samples as in Figs. 2, 3 and 4). Numbers refer to demagnetization temperatures in °C.

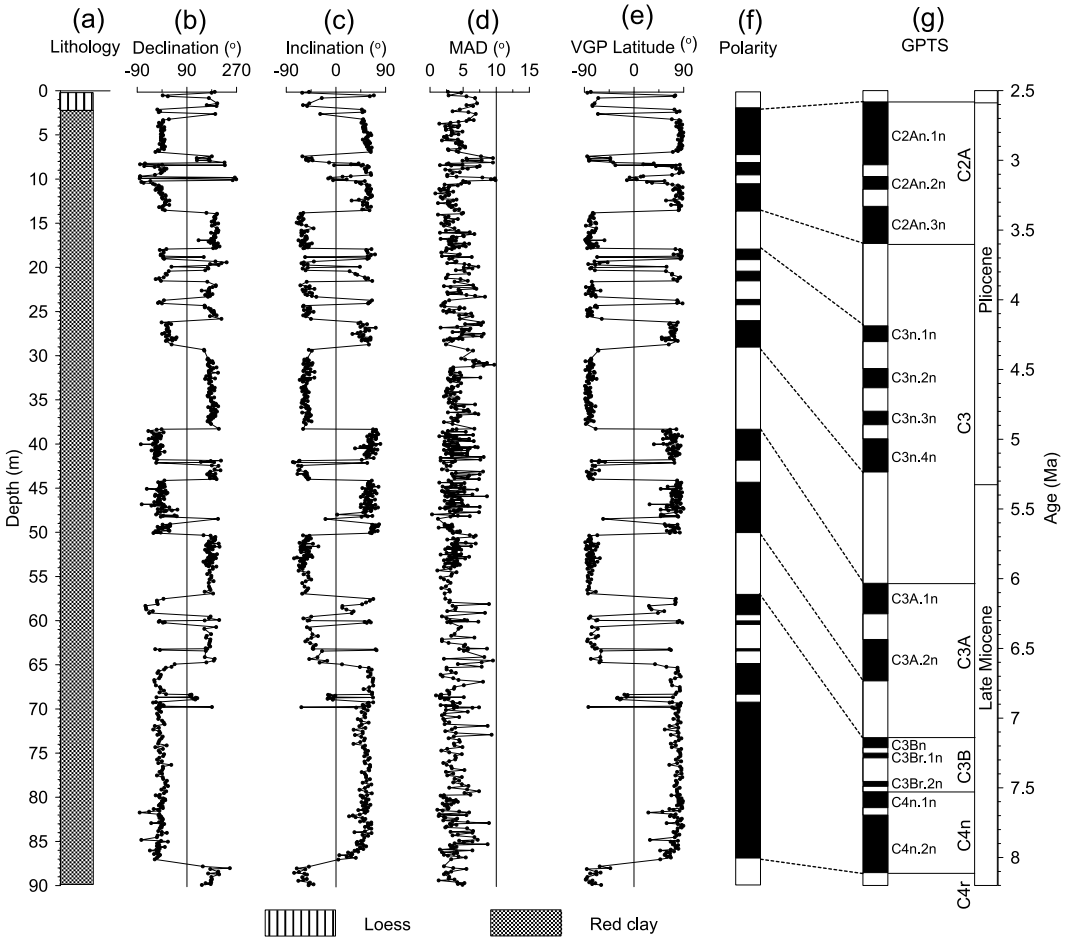

Fig. 6. Lithostratigraphy and magnetostratigraphy of the Shilou section and correlation to the geomagnetic polarity timescale (GPTS). (a) Simplified lithology, (b) paleomagnetic declination, (c) inclination, and (d) maximum angular deviation (MAD) of the characteristic remanent magnetization, (e) virtual geomagnetic pole (VGP) latitude, and (f) paleomagnetic polarity for the Shilou section with proposed correlation to the GPTS. (g) GPTS (Hilgen et al., 2012) for the period of interest.

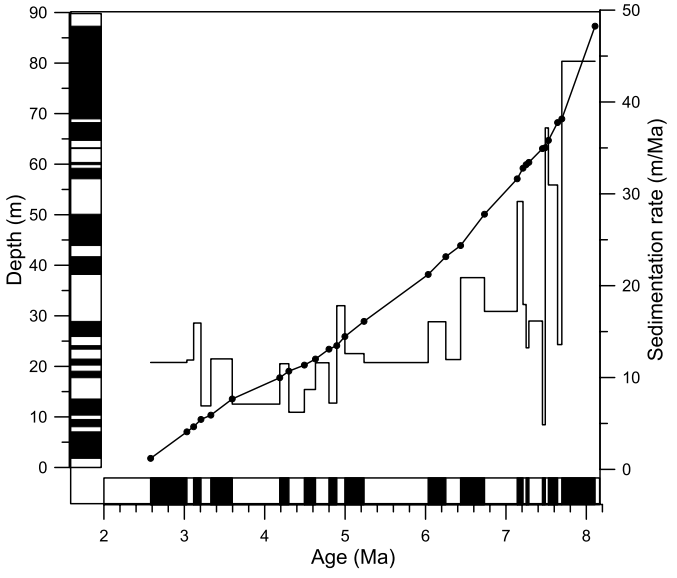

Fig. 7. Stratigraphic depth and sedimentation rate plotted versus magnetostratigraphic ages to illustrate the sedimentation process for the Shilou Red Clay sequence. The polarity time scale is that of Hilgen et al. (2012).

polarity divisions, our results enable unequivocal correlation to the GPTS (Hilgen et al., 2012). The age of the base of the Shilou Red Clay is reassigned to ~8.2 Ma, in contrast to the previously inferred ~11 Ma (Xu et al., 2009) (Figs. 6 and 10). This new age assignment (8.2–2.6 Ma) is consistent with results from other Red Clay sequences on the central and eastern Loess Plateau, such as the Xifeng, Chaona, Lingtai and Jiaxian sections, which range in age from 2.6 Ma to 8–7 Ma (Sun et al., 1998a; Ding et al., 1999; Qiang et al., 2001; Song et al., 2001).

Two hypotheses have been used to explain the documented EASM intensification. One hypothesis involves closure of the Panama Seaway (Nie et al., 2014), which is thought to have resulted in freshening of Eastern Equatorial and North Pacific surface water since ~4.8 Ma (Haug et al., 2001; Nie et al., 2014). This freshening may have then led to sea ice formation in the North Pacific Ocean, which enhanced the high-pressure cell over the Pacific (Driscoll and Haug, 1998; Nie et al., 2014). As a result, southerly and southeasterly winds would have been enhanced, which would intensify EASM precipitation (Nie et al., 2014). However, this scenario can only explain a short-duration shift in EASM intensity within the Pliocene.

The other hypothesis attributes EASM intensification to growth of the Tibetan Plateau (Prell and Kutzbach, 1992; An et al., 2001). Climate simulations indicate that this tectonic process had profound effects on EASM initiation and development (Prell and Kutzbach, 1992; An et al., 2001; Boos and Kuang, 2010), but it largely occurred from the Eocene to the Mid-Miocene (Rowley and Currie, 2006; Xiao et al., 2012; Wang et al., 2014) and, therefore, pre-dates the time interval studied here. The eastern and northern margins of the Tibetan Plateau may have risen slightly during certain intervals of the Late Miocene–Pliocene (Zheng et al., 2000;

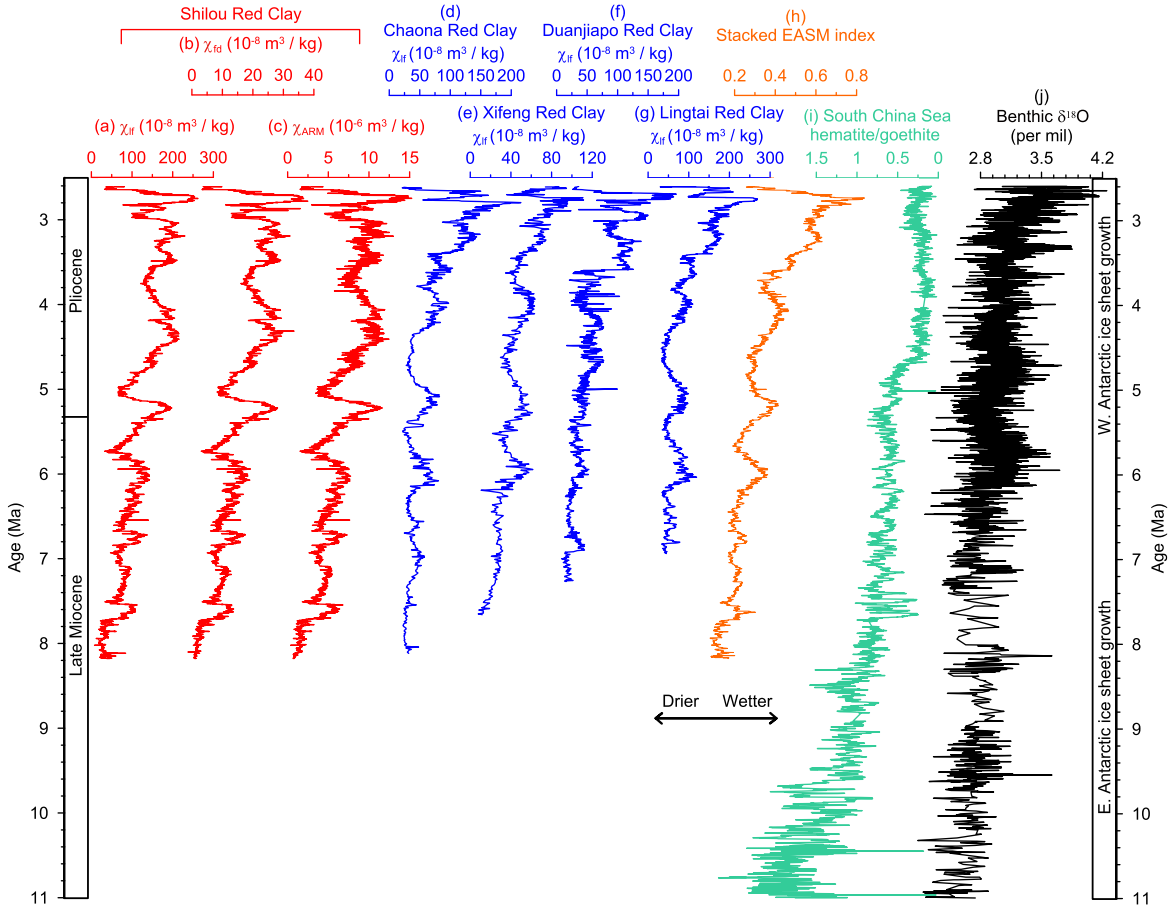

Fig. 8. Late Miocene–Pliocene EASM evolution. Stratigraphic variations of (a) χ_{lf}, (b) χ_{fd} and (c) χ_{ARM} for the Shilou Red Clay sequence. Stratigraphic variations of χ_{lf} for the Red Clay sequences from (d) Chaona (Nie et al., 2007), (e) Xifeng (Sun et al., 1998a), (f) Duanjiapo (An et al., 2000) and (g) Lingtai (Sun et al., 2010). The chronology for all of the Red Clay sequences was obtained from magnetostratigraphic age models. (h) Stacked EASM record based on χ_{lf} data from the Shilou, Chaona, Xifeng, Duanjiapo and Lingtai Red Clay sections. We combined the five χ_{lf} records by normalizing each to unit variance (between 0 and 1) and averaging to produce a stacked EASM record, which captures consistent long-term variability and minimizes issues related to short-term chronological misalignments and regional differences. A distinct upward increasing trend in the stack indicates continued EASM intensification through the Late Miocene–Pliocene. (i) Hematite/goethite ratio from South China Sea sediments (Clift, 2006), with a long-term decreasing trend from ca 11 to 2.6 Ma, which indicates increasing EASM intensity. (j) Stacked deep-sea benthic foraminiferal oxygen isotope curve based on data from Deep Sea Drilling Project and Ocean Drilling Program sites (Zachos et al., 2008), with a long-term increasing trend from 11 to 2.6 Ma. Major ice sheets expanded in East and West Antarctica at ca 11 and 6–5 Ma, respectively (Zachos et al., 2001).

Charreau et al., 2005; Molnar, 2005; An et al., 2006); however, it is controversial whether intermittent, regional and limited uplift would have intensified the EASM (Boos and Kuang, 2010). Recent climate simulations indicate that after formation of the Himalayas and adjacent mountain ranges, subsequent northward and eastward growth of the Tibetan Plateau would have had little impact on the Asian summer monsoon (Boos and Kuang, 2010). Furthermore, even if the Tibetan Plateau had reached a significant altitude before the Late Miocene and had intensified the EASM, it may not account for continued EASM intensification through the Late Miocene–Pliocene, although we cannot exclude intermittent influences of the Tibetan Plateau on climate during some short time intervals. Therefore, we propose a new mechanism involving Antarctic glaciation to interpret the observed long-term trend of enhanced EASM during the Late Miocene and Pliocene.

Southern hemisphere atmospheric circulation, in particular the Australian high, plays an important role in seasonal EASM establishment and in its northward advance (He et al., 1991; Xue et al., 2003; Clemens et al., 2008; Rohling et al., 2009) (Fig. 1). Modern observations indicate that southern hemisphere winter circulation commences in the lower troposphere by the end of March (Xue et al., 2003). Through cross-equatorial currents, this leads to establishment of EASM circulation (Xue et al., 2003). As the southern hemisphere cools, atmospheric meridional circulation over Australia intensifies. This strengthens the Australian high and lower tropospheric cross-equatorial air flow (He et al., 1991). Subsequently, this creates stronger southerly winds in East Asia, concomitant with a more prominent low pressure cell in Asia: an intensified cross-equatorial pressure gradient is established between the Australian high and Asian low. As a result, the Intertropical Convergence Zone and Asian monsoon rain belt move northward (Wang, 2006; Holbourn et al., 2010), with attendant increased moisture transportation from the tropical oceans. In contrast to northern hemisphere cooling, southern hemisphere cooling and an associated strengthened Australian high can enhance the southern Hadley cell, weaken the northern Hadley cell and move the ascending branch of the Hadley cell northward (Chiang and Friedman, 2012). This altered Hadley circulation can induce greater energy and moisture transport from the tropical oceans to continental Asia. In addition, a cooler southern hemisphere (relative to a warmer northern hemisphere) is associated with preferential surface water cooling in the southwestern equatorial Pacific. This enhances the zonal sea-surface temperature (SST) gradient in the tropical oceans, equatorial southerly winds, and in turn EASM circulation (Holbourn et al., 2010). Therefore, both atmospheric and oceanic modulations due to southern hemisphere cooling help to intensify the EASM via enhancing the zonal SST gradient and cross-equatorial pressure gradient between low pressures

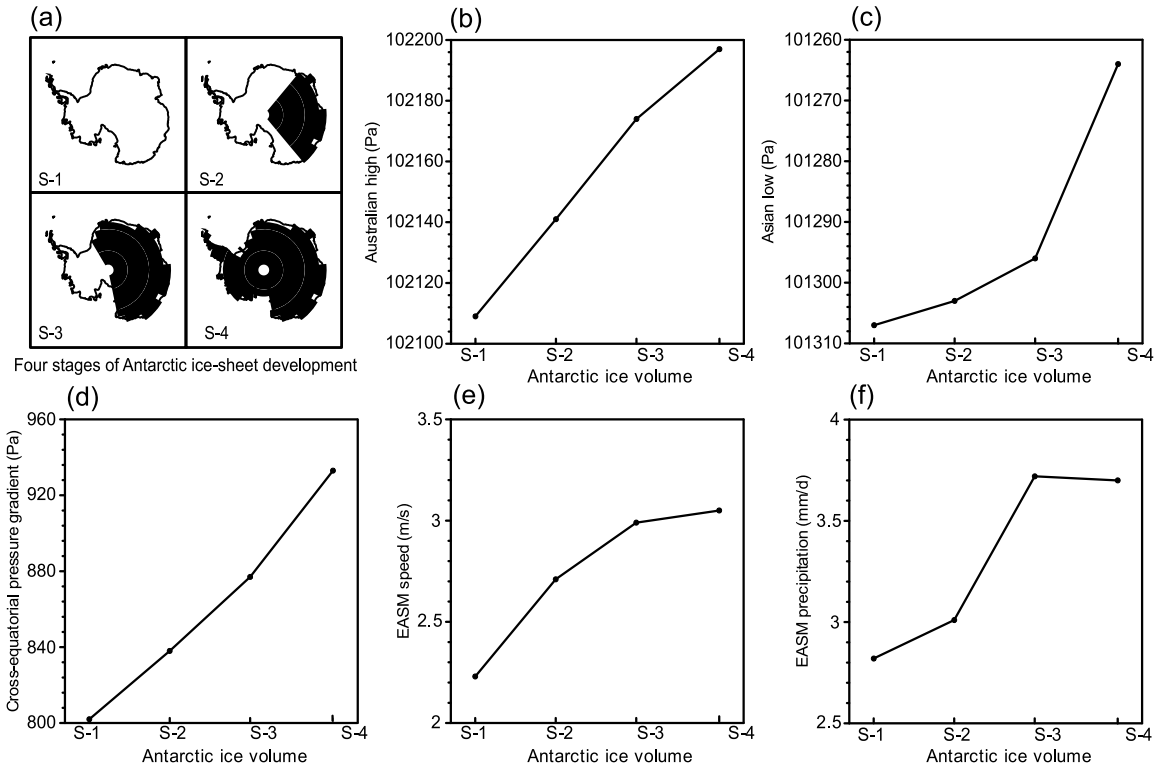

Fig. 9. Simulated EASM responses to four idealized stepwise increases in ice-sheet size from East to West Antarctica. (a) Four scenarios of Antarctic ice-sheet development. Scenarios S-1, S-2, S-3 and S-4 represent 0%, 33%, 66% and 100% of the present Antarctic ice cover, increasing in size from East to West. Variations in (b) Australian high, (c) Asian low, (d) cross-equatorial pressure gradient between the Australian high (120–150°E, 20–35°S) and Asian low (80–110°E, 25–40°N), (e) wind speed, and (f) precipitation averaged for June–July–August in the EASM area (105–120°E, 20–40°N).

over mid-latitude Asia and high pressures over Australia. Similar inter-hemispheric climate dynamics have been proposed to explain Quaternary millennial- to orbital-scale monsoon variability (Rohling et al., 2009; An et al., 2011).

In contrast to Quaternary ice ages, when major ice sheets were present in both hemispheres, Late Miocene–Pliocene ice sheets are thought to have been primarily restricted to Antarctica, with only relatively small northern hemisphere ice expansions (Zachos et al., 2001; Clemens et al., 2008). Furthermore, it is commonly inferred from a trend to increasingly heavy oxygen isotopic compositions (δ^{18}O) of deep-sea benthic foraminifera (Fig. 8j) that Antarctic ice sheets underwent long-term expansion from 11 to 2.6 Ma, with establishment of sustained major ice sheets in East Antarctica by ~11 Ma and additional West Antarctic ice-sheet expansion by 6–5 Ma (Zachos et al., 2001, 2008). This Antarctic ice-sheet development parallels the gradual EASM intensification (Fig. 8), which supports our inference of an important inter-hemispheric link between them. Although intricacies concerning the proportionality of ice-volume, temperature, and benthic δ^{18}O changes as well as the additional influence of northern hemisphere ice sheets during the Late Pliocene are debated (Zachos et al., 2001; Rohling et al., 2014), increasing Antarctic ice volume and decreasing Antarctic temperatures would have resulted in fundamental changes in atmospheric convection and oceanic circulation in tropical and middle latitudes. Reorganization of atmospheric and oceanic patterns, such as an altered Hadley circulation and enhanced cross-equatorial SST and atmospheric pressure gradients following Late Miocene–Pliocene ice growth episodes in Antarctica, would have driven EASM intensification, similar to the present-day and Quaternary situations (He et al., 1991; Rohling et al., 2009; An et al., 2011).

Our inference of inter-hemispheric coupling based on temporal agreement between EASM intensification and Antarctic ice-sheet growth (Fig. 8) is borne out by our numerical climate-model assessments of EASM responses to an idealized stepwise increase in ice-sheet size from East to West Antarctica (Fig. 9 and Fig. S1). These results suggest clearly that increasing ice-sheet sizes in East Antarctica, and later in Central and West Antarctica, would have caused intensification of EASM precipitation and wind velocities. The main underlying processes are an increase in the Australian high pressure cell, and deepening of the Asian low pressure cell, along with an enhanced cross-equatorial pressure gradient between these two features (Fig. 9).

We also note that the long-term influence of Antarctic glaciation on EASM intensification is not linear, and may contain spatial differences (Figs. 8–9 and Fig. S1). Although the climate-model simulation indicates that Late Pliocene growth of the West Antarctic ice sheet may have resulted in a strongly enhanced cross-equatorial pressure gradient, no obvious increase is found in simulated averaged EASM precipitation (Fig. 9). Magnetic proxy records from the Chinese Loess Plateau indicate considerably increased EASM precipitation, while hematite/goethite ratios from the South China Sea indicate a small long-term change in EASM precipitation (Fig. 8). Such differences could result from additional environmental influences, such as closure of the Panama Seaway (Li et al., 2008; Nie et al., 2008b, 2014), regional growth of the Tibetan Plateau (Prell and Kutzbach, 1992; An et al., 2001; Liu and Dong, 2013) and/or increases in northern hemisphere ice volume (Zachos et al., 2001). These changes superimposed on the effects of long-term Antarctic glaciation would have led to more complicated monsoon responses.

6. Conclusions

New magnetostratigraphic results suggest that the Shilou eolian Red Clay sequence on the eastern Chinese Loess Plateau spans from ~8.2 to 2.6 Ma, in contrast to the previously inferred 11–2.6 Ma. New mineral magnetic records of the Shilou Red Clay, which por-

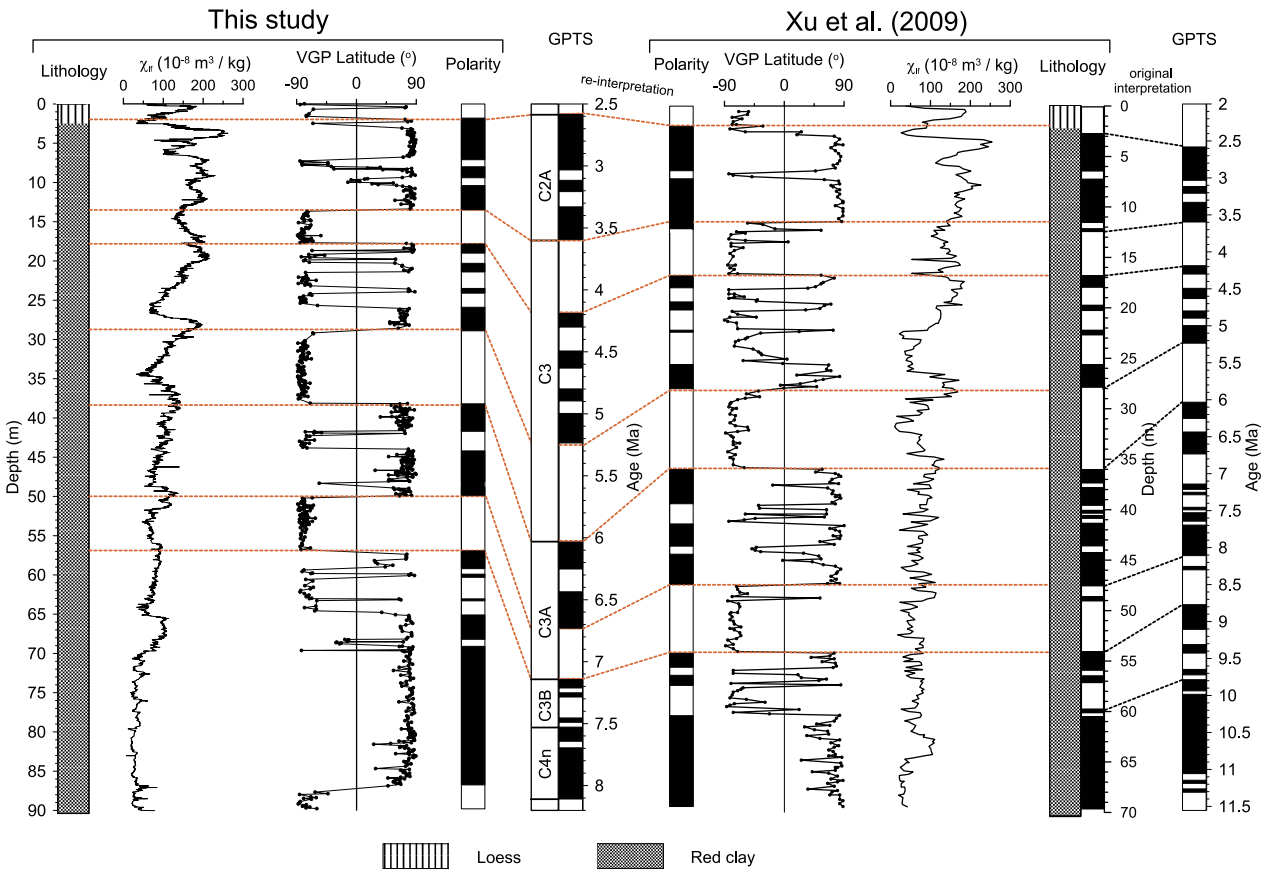

Fig. 10. Comparison of the Shilou Red Clay magnetostratigraphic records from this study and the earlier study (Xu et al., 2009). The χ_{lf} record for the previously studied section is from Xu et al. (2012). The section studied here lies ~1 km west of the previously studied section. Magnetostratigraphic data are summarized as VGP latitudes. Xu et al. (2009) suggested an age range of 11–2.6 Ma for the Shilou Red Clay (right-hand side). Our new high-resolution results (left-hand side) improve the definition of polarity divisions, which enable unequivocal correlation to the GPTS, and reassignment of the age of the base of the Shilou Red Clay to ~8.2 Ma in contrast with the previously inferred ~11 Ma (Xu et al., 2009). This improvement leads to a more reasonable re-interpretation of the previous magnetostratigraphy between ca 8 and 2.6 Ma (cf. magnetostratigraphic correlations in the center of the figure).

tray EASM evolution, indicate a long-term trend of an enhanced EASM from 8.2 to 2.6 Ma. We infer from both proxy data and a numerical climate-model assessment that changes in Antarctic glaciation were an important driver of long-term Late Miocene–Pliocene EASM intensification. Stepwise increase in ice-sheet size from East to West Antarctica caused intensification of the cross-equatorial pressure gradient between a high-pressure cell over Australia and a low-pressure cell over mid-latitude East Asia, as well as intensification of the cross-equatorial SST gradient. These combined atmospheric and oceanic adjustments led to EASM intensification. This new hypothesis is consistent with the importance of southern hemisphere processes for present-day monsoon dynamics on short (seasonal) timescales, and previous (mostly qualitative) interpretations of Quaternary Asian monsoon changes on millennial and orbital timescales.

Acknowledgements

We thank Peter Clift, Peter Molnar, Leping Yue, Qingsong Liu and two anonymous reviewers for their suggestions and comments that helped to improve the paper and Peng Zhang, Shan Lin, Zhaoxia Jiang and Suzhen Liu for their help during the laboratory work. This study was financially supported by the National Natural Science Foundation of China (grants 41290253 and 41290255), the National Basic Research Program of China (grant 2013CB956402) and the Australian Research Council (2012 Australian Laureate Fellowship FL120100050 and DP110105419).

Appendix A. Supplementary material

Supplementary material related to this article can be found online at http://dx.doi.org/10.1016/j.epsl.2016.03.028.

References

An, Z.S., 2000. The history and variability of the East Asian paleomonsoon climate. Quat. Sci. Rev. 19, 171–187.
An, Z.S., 2014. Late Cenozoic Climate Change in Asia: Loess, Monsoon and Monsoon-Arid Environment Evolution. Springer, Amsterdam.
An, Z.S., Liu, T.S., Lu, Y.C., Porter, S.C., Kukla, G., Wu, X.H., Hua, Y.M., 1990. The long-term paleomonsoon variation recorded by the loess–paleosol sequence in central China. Quat. Int. 7–8, 91–95.
An, Z.S., Kukla, G.J., Porter, S.C., Xiao, J.L., 1991. Magnetic susceptibility evidence of monsoon variation on the loess plateau of central China during the last 130,000 years. Quat. Res. 36, 29–36.
An, Z.S., Sun, D.H., Chen, M.Y., Sun, Y.B., Li, L., Chen, B.Q., 2000. Red clay sequences in Chinese Loess Plateau and recorded paleoclimate events of the late Tertiary. Quat. Sci. 20, 435–446 (in Chinese with English abstract).
An, Z.S., Kutzbach, J.E., Prell, W.L., Porter, S.C., 2001. Evolution of Asian monsoons and phased uplift of the Himalayan Tibetan plateau since Late Miocene times. Nature 411, 62–66.
An, Z.S., Zhang, P.Z., Wang, E., Wang, S.M., Qiang, X.K., Li, L., Song, Y.G., Chang, H., Liu, X.D., Zhou, W.J., Liu, W.G., Cao, J.J., Li, X.Q., Shen, J., Liu, Y., Ai, L., 2006. Changes of the monsoon-arid environment in China and growth of the Tibetan Plateau since the Miocene. Quat. Sci. 26, 678–693 (in Chinese with English abstract).
An, Z.S., Clemens, S.C., Shen, J., Qiang, X.K., Jin, Z.D., Sun, Y.B., Prell, W.L., Luo, J.J., Wang, S.M., Xu, H., Cai, Y.J., Zhou, W.J., Liu, X.D., Liu, W.G., Shi, Z.G., Yan, L.B., Xiao, X.Y., Chang, H., Wu, F., Ai, L., Lu, F.Y., 2011. Glacial–interglacial Indian summer monsoon dynamics. Science 333, 719–723.
An, Z.S., Wu, G.X., Li, J.P., Sun, Y.B., Liu, Y.M., Zhou, W.J., Cai, Y.J., Duan, A.M., Li, L., Mao, J.Y., Cheng, H., Shi, Z.G., Tan, L.C., Yan, H., Ao, H., Chang, H., Feng, J., 2015.

Global monsoon dynamics and climate change. Annu. Rev. Earth Planet. Sci. 43, 29–77.
Boos, W.R., Kuang, Z.M., 2010. Dominant control of the South Asian monsoon by orographic insulation versus plateau heating. Nature 463, 218–222.
Charreau, J., Chen, Y., Gilder, S., Dominguez, S., Avouac, J.P., Sen, S., Sun, D.J., Li, Y.G., Wang, W.M., 2005. Magnetostratigraphy and rock magnetism of the Neogene Kuitun He section (northwest China): implications for Late Cenozoic uplift of the Tianshan mountains. Earth Planet. Sci. Lett. 230, 177–192.
Chiang, J.C.H., Friedman, A.R., 2012. Extratropical cooling, interhemispheric thermal gradients, and tropical climate change. Annu. Rev. Earth Planet. Sci. 40, 383–412.
Clemens, S.C., Prell, W.L., Sun, Y.B., Liu, Z.Y., Chen, G.S., 2008. Southern Hemisphere forcing of Pliocene $\delta^{18}O$ and the evolution of Indo-Asian monsoons. Paleoceanography 23, PA4210. http://dx.doi.org/10.1029/2008PA001638.
Clift, P.D., 2006. Controls on the erosion of Cenozoic Asia and the flux of clastic sediment to the ocean. Earth Planet. Sci. Lett. 241, 571–580.
Clift, P.D., Plumb, R.A., 2008. The Asian Monsoon: Causes, History and Effects. Cambridge University Press, Cambridge.
Collins, W.D., Rasch, P.J., Boville, B.A., Hack, J.J., McCaa, J.R., Williamson, D.L., Kiehl, J.T., Briegleb, B., Bitz, C., Lin, S.L., Zhang, M., Dai, Y., 2004. Description of the NCAR community atmosphere model (CAM 3.0). Technical Note TN-464+STR. National Center for Atmospheric Research, Colorado, USA.
Dee, D.P., Uppala, S.M., Simmons, A.J., Berrisford, P., Poli, P., Kobayashi, S., Andrae, U., Balmaseda, M.A., Balsamo, G., Bauer, P., Bechtold, P., Beljaars, A.C.M., van de Berg, L., Bidlot, J., Bormann, N., Delsol, C., Dragani, R., Fuentes, M., Geer, A.J., Haimberger, L., Healy, S.B., Hersbach, H., Hólm, E.V., Isaksen, L., Kållberg, P., Köhler, M., Matricardi, M., McNally, A.P., Monge-Sanz, B.M., Morcrette, J.-J., Park, B.-K., Peubey, C., de Rosnay, P., Tavolato, C., Thépaut, J.-N., Vitart, F., 2011. The ERA-Interim reanalysis: configuration and performance of the data assimilation system. Q. J. R. Meteorol. Soc. 137, 553–597.
deMenocal, P.B., Rind, D., 1993. Sensitivity of Asian and African climate to variations in seasonal insolation, glacial ice cover, sea surface temperature, and Asian orography. J. Geophys. Res. 98, 7265–7287.
Ding, Z.L., Liu, T.S., Rutter, N.W., Yu, Z.W., Guo, Z.T., Zhu, R.X., 1995. Ice-volume forcing of East Asian winter monsoon variations in the past 800,000 years. Quat. Res. 44, 149–159.
Ding, Z.L., Xiong, S.F., Sun, J.M., Yang, S.L., Gu, Z.Y., Liu, T.S., 1999. Pedostratigraphy and paleomagnetism of a ~7.0 Ma eolian loess–red clay sequence at Lingtai, Loess Plateau, north-central China and the implications for paleomonsoon evolution. Palaeogeogr. Palaeoclimatol. Palaeoecol. 152, 49–66.
Driscoll, N.W., Haug, G.H., 1998. A short circuit in thermohaline circulation: a cause for northern hemisphere glaciation? Science 282, 436–438.
Dunlop, D.J., Özdemir, Ö., 1997. Rock Magnetism: Fundamentals and Frontiers. Cambridge University Press, Cambridge.
Egli, R., Chen, A.P., Winklhofer, M., Kodama, K.P., Horng, C.S., 2010. Detection of noninteracting single domain particles using first-order reversal curve diagrams. Geochem. Geophys. Geosyst. 11, Q01Z11. http://dx.doi.org/10.1029/2009GC002916.
Evans, M.E., Heller, F., 2001. Magnetism of loess/palaeosol sequences: recent developments. Earth-Sci. Rev. 54, 129–144.
Evans, M.E., Heller, F., 2003. Environmental Magnetism: Principles and Applications of Enviromagnetics. Academic Press, Manhattan, New York.
Guo, Z.T., Ruddiman, W.F., Hao, Q.Z., Wu, H.B., Qiao, Y.S., Zhu, R.X., Peng, S.Z., Wei, J.J., Yuan, B.Y., Liu, T.S., 2002. Onset of Asian desertification by 22 Myr ago inferred from loess deposits in China. Nature 416, 159–163.
Hao, Q.Z., Guo, Z.T., 2005. Spatial variations of magnetic susceptibility of Chinese loess for the last 600 kyr: implications for monsoon evolution. J. Geophys. Res. 110, B12101. http://dx.doi.org/10.1029/2005JB003765.
Hao, Q.Z., Oldfield, F., Bloemendal, J., Guo, Z.T., 2008. The magnetic properties of loess and paleosol samples from the Chinese Loess Plateau spanning the last 22 million years. Palaeogeogr. Palaeoclimatol. Palaeoecol. 260, 389–404.
Haug, G.H., Tiedemann, R., Zahn, R., Ravelo, A.C., 2001. Role of Panama uplift on oceanic freshwater balance. Geology 29, 207–210.
He, J.H., Li, J., Li, Y.P., 1991. The influence of cold air activities over Australia on east Asian summer monsoon – a numerical experiment. Acta Meterol. Sin. 49, 162–169 (in Chinese).
Heller, F., Evans, M.E., 1995. Loess magnetism. Rev. Geophys. 33, 211–240.
Heller, F., Liu, T.S., 1984. Magnetism of Chinese loess deposits. Geophys. J. Int. 77, 125–141.
Heller, F., Liu, T.S., 1986. Palaeoclimate and sedimentary history from magnetic susceptibility of loess in China. Geophys. Res. Lett. 13, 1169–1172.
Hilgen, F.J., Lourens, L.J., van Dam, J.A., 2012. The Neogene period. In: Gradstein, F.M., Ogg, J.G., Schmitz, M., Ogg, G. (Eds.), The Geologic Time Scale. Elsevier, Amsterdam, pp. 923–978.
Holbourn, A., Kuhnt, W., Regenberg, M., Schulz, M., Mix, A., Andersen, N., 2010. Does Antarctic glaciation force migration of the tropical rain belt? Geology 38, 783–786.
Hunt, C.P., Banerjee, S.K., Han, J.M., Solheid, P.A., Oches, E., Sun, W.W., Liu, T.S., 1995. Rock-magnetic proxies of climate change in the loess–paleosol sequences of the western Loess Plateau of China. Geophys. J. Int. 123, 232–244.
Jia, G.D., Peng, P.A., Zhao, Q.H., Jian, Z.M., 2003. Changes in terrestrial ecosystem since 30 Ma in East Asia: stable isotope evidence from black carbon in the South China Sea. Geology 31, 1093–1096.
Jones, C.H., 2002. User-driven integrated software lives: "Paleomag" paleomagnetics analysis on the Macintosh. Comput. Geosci. 28, 1145–1151.
Kirschvink, J.L., 1980. The least-squares line and plane and the analysis of palaeomagnetic data. Geophys. J. R. Astron. Soc. 62, 699–718.
Kruiver, P.P., Dekkers, M.J., Heslop, D., 2001. Quantification of magnetic coercivity components by the analysis of acquisition curves of isothermal remanent magnetisation. Earth Planet. Sci. Lett. 189, 269–276.
Li, F.J., Rousseau, D.D., Wu, N.Q., Hao, Q.Z., Pei, Y.P., 2008. Late Neogene evolution of the East Asian monsoon revealed by terrestrial mollusk record in Western Chinese Loess Plateau: from winter to summer dominated sub-regime. Earth Planet. Sci. Lett. 274, 439–447.
Liu, Q.S., Deng, C.L., Torrent, J., Zhu, R.X., 2007. Review of recent developments in mineral magnetism of the Chinese loess. Quat. Sci. Rev. 26, 368–385.
Liu, Q.S., Roberts, A.P., Larrasoaña, J.C., Banerjee, S.K., Guyodo, Y., Tauxe, L., Oldfield, F., 2012. Environmental magnetism: principles and applications. Rev. Geophys. 50, RG4002. http://dx.doi.org/10.1029/2012RG000393.
Liu, Q.S., Jin, C.S., Hu, P.X., Jiang, Z.X., Ge, K.P., Roberts, A.P., 2015. Magnetostratigraphy of Chinese loess–paleosol sequences. Earth-Sci. Rev. 150, 139–167.
Liu, T.S., 1985. Loess and the Environment. China Ocean Press, Beijing.
Liu, T.S., Ding, Z.L., 1998. Chinese loess and the paleomonsoon. Annu. Rev. Earth Planet. Sci. 26, 111–145.
Liu, X.D., Dong, B.W., 2013. Influence of the Tibetan Plateau uplift on the Asian monsoon-arid environment evolution. Chin. Sci. Bull. 58, 4277–4291.
Liu, X.M., Rolph, T., An, Z.S., Hesse, P., 2003. Paleoclimatic significance of magnetic properties on the Red Clay underlying the loess and paleosols in China. Palaeogeogr. Palaeoclimatol. Palaeoecol. 199, 153–166.
Maher, B.A., Thompson, R., 1995. Paleorainfall reconstructions from pedogenic magnetic susceptibility variations in the Chinese loess and paleosols. Quat. Res. 44, 383–391.
Molnar, P., 2005. Mio-Pliocene growth of the Tibetan Plateau and evolution of East Asian climate. Palaeontol. Electronica 8, 1–23.
Muxworthy, A.R., Dunlop, D.J., 2002. First-order reversal curve (FORC) diagrams for pseudo-single-domain magnetites at high temperature. Earth Planet. Sci. Lett. 203, 369–382.
Nie, J.S., King, J.W., Fang, X.M., 2007. Enhancement mechanisms of magnetic susceptibility in the Chinese red-clay sequence. Geophys. Res. Lett. 341, L19705. http://dx.doi.org/10.1029/2007GL031430.
Nie, J.S., King, J., Jackson, M., Fang, X.M., Song, Y.G., 2008a. AC magnetic susceptibility studies of Chinese red clay sediments between 4.8 and 4.1 Ma: paleoceanographic and paleoclimatic implications. J. Geophys. Res. 113, B10106. http://dx.doi.org/10.1029/2008JB005654.
Nie, J.S., King, J.W., Fang, X.M., 2008b. Link between benthic oxygen isotopes and magnetic susceptibility in the red-clay sequence on the Chinese Loess Plateau. Geophys. Res. Lett. 35, L03703. http://dx.doi.org/10.1029/2007GL032817.
Nie, J.S., Song, Y.G., King, J.W., Fang, X.M., Heil, C., 2010. HIRM variations in the Chinese red-clay sequence: insights into pedogenesis in the dust source area. J. Asian Earth Sci. 38, 96–104.
Nie, J.S., Stevens, T., Song, Y.G., King, J.W., Zhang, R., Ji, S.C., Gong, L.S., Cares, D., 2014. Pacific freshening drives Pliocene cooling and Asian monsoon intensification. Sci. Rep. 4, 5474. http://dx.doi.org/10.1038/srep05474.
Oldfield, F., 1991. Environmental magnetism – a personal perspective. Quat. Sci. Rev. 10, 73–85.
Pike, C.R., Roberts, A.P., Verosub, K.L., 2001. First-order reversal curve diagrams and thermal relaxation effects in magnetic particles. Geophys. J. Int. 145, 721–730.
Prell, W.L., Kutzbach, J.E., 1992. Sensitivity of the Indian Monsoon to forcing parameters and implications for its evolution. Nature 360, 647–652.
Qiang, X.K., Li, Z.X., Powell, C.M., Zheng, H.B., 2001. Magnetostratigraphic record of the Late Miocene onset of the East Asian monsoon, and Pliocene uplift of northern Tibet. Earth Planet. Sci. Lett. 187, 83–93.
Qiang, X.K., An, Z.S., Song, Y.G., Chang, H., Sun, Y.B., Liu, W.G., Ao, H., Dong, J.B., Fu, C.F., Wu, F., Lu, F.Y., Cai, Y.J., Zhou, W.J., Cao, J.J., Xu, X.W., Ai, L., 2011. New eolian red clay sequence on the western Chinese Loess Plateau linked to onset of Asian desertification about 25 Ma ago. Sci. China Earth Sci. 54, 136–144.
Roberts, A.P., 2015. Magnetic mineral diagenesis. Earth-Sci. Rev. 151, 1–47.
Roberts, A.P., Pike, C.R., Verosub, K.L., 2000. First-order reversal curve diagrams: a new tool for characterizing the magnetic properties of natural samples. J. Geophys. Res. 105, 28461–28475.
Roberts, A.P., Heslop, D., Zhao, X., Pike, C.R., 2014. Understanding fine magnetic particle systems through use of first-order reversal curve diagrams. Rev. Geophys. 52, 557–602.
Rohling, E.J., Liu, Q.S., Roberts, A.P., Stanford, J.D., Rasmussen, S.O., Langen, P.L., Siddall, M., 2009. Controls on the East Asian monsoon during the last glacial cycle, based on comparison between Hulu Cave and polar ice-core records. Quat. Sci. Rev. 28, 3291–3302.
Rohling, E.J., Foster, G.L., Grant, K.M., Marino, G., Roberts, A.P., Tamisiea, M.E., Williams, F., 2014. Sea-level and deep-sea-temperature variability over the past 5.3 million years. Nature 508, 477–482.

Rowley, D.B., Currie, B.S., 2006. Palaeo-altimetry of the late Eocene to Miocene Lunpola basin, central Tibet. Nature 439, 677–681.
Song, Y.G., Fang, X.M., Li, J.J., An, Z.S., Miao, X.D., 2001. The Late Cenozoic uplift of the Liupan Shan, China. Sci. China Earth Sci. 44, 176–184.
Sun, D.H., Liu, D.S., Liu, T.S., Chen, M.Y., An, Z.S., Shaw, J., 1997. Magnetostratigraphy and palaeoclimate of Red Clay sequences from Chinese Loess Plateau. Sci. China 40, 337–343.
Sun, D.H., An, Z.S., Shaw, J., Bloemendal, J., Sun, Y.B., 1998a. Magnetostratigraphy and palaeoclimatic significance of late tertiary aeolian sequences in the Chinese Loess Plateau. Geophys. J. Int. 134, 207–212.
Sun, D.H., Shaw, J., An, Z.S., Cheng, M.Y., Yue, L.P., 1998b. Magnetostratigraphy and paleoclimatic interpretation of a continuous 7.2 Ma Late Cenozoic eolian sediments from the Chinese Loess Plateau. Geophys. Res. Lett. 25, 85–88.
Sun, Y.B., An, Z.S., Clemens, S., Bloemendal, J., Vandenberghe, J., 2010. Seven million years of wind and precipitation variability on the Chinese Loess Plateau. Earth Planet. Sci. Lett. 297, 525–535.
Sun, Y.B., Kutzbach, J., An, Z.S., Clemens, S., Liu, Z.Y., Liu, W.G., Liu, X.D., Shi, Z.G., Zheng, W.P., Liang, L.J., Yan, Y., Li, Y., 2015. Astronomical and glacial forcing of East Asian summer monsoon variability. Quat. Sci. Rev. 115, 132–142.
Verosub, K.L., Roberts, A.P., 1995. Environmental magnetism: past, present, and future. J. Geophys. Res. 100, 2175–2192.
Wang, B., 2006. The Asian Monsoon. Springer, Berlin.
Wang, B., Zheng, H.B., He, Z., Wang, P., Kaakinen, A., Zhou, X.Y., 2014. Middle Miocene eolian sediments on the southern Chinese Loess Plateau dated by magnetostratigraphy. Palaeogeogr. Palaeoclimatol. Palaeoecol. 411, 257–266.
Webster, P.J., Magana, V.O., Palmer, T.N., Shukla, J., Tomas, R.A., Yanai, M., Yasunari, T., 1998. Monsoons: processes, predictability, and the prospects for prediction. J. Geophys. Res. 103, 14451–14510.
Xiao, G.Q., Guo, Z.T., Dupont-Nivet, G., Lu, H.Y., Wu, N.Q., Ge, J.Y., Hao, Q.Z., Peng, S.Z., Li, F.J., Abels, H.A., Zhang, K.X., 2012. Evidence for northeastern Tibetan Plateau uplift between 25 and 20 Ma in the sedimentary archive of the Xining Basin, Northwestern China. Earth Planet. Sci. Lett. 317, 185–195.
Xu, Y., Yue, L.P., Li, J.X., Sun, L., Sun, B., Zhang, J.Y., Ma, J., Wang, J.Q., 2009. An 11-Ma-old red clay sequence on the Eastern Chinese Loess Plateau. Palaeogeogr. Palaeoclimatol. Palaeoecol. 284, 383–391.
Xu, Y., Yue, L.P., Li, J.X., Sun, L., Sun, B., Zhang, J.Y., Ma, J., Wang, J.Q., 2012. Red clay deposits on the Chinese Loess Plateau during 11.0–2.6 Ma and its implications for long-term evolution of East Asian monsoon. Environ. Earth Sci. 66, 2021–2030.
Xue, F., Wang, H.J., He, J.H., 2003. Interannual variability of Mascarene high and Australian high and their influences on summer rainfall over East Asia. Chin. Sci. Bull. 48, 492–497.
Yang, S.L., Ding, Z.L., Li, Y.Y., Wang, X., Jiang, W.Y., Huang, X.F., 2015. Warming-induced northwestward migration of the East Asian monsoon rain belt from the Last Glacial Maximum to the mid-Holocene. Proc. Natl. Acad. Sci. USA 112, 13178–13183.
Zachos, J., Pagani, M., Sloan, L., Thomas, E., Billups, K., 2001. Trends, rhythms, and aberrations in global climate 65 Ma to present. Science 292, 686–693.
Zachos, J.C., Dickens, G.R., Zeebe, R.E., 2008. An early Cenozoic perspective on greenhouse warming and carbon-cycle dynamics. Nature 451, 279–283.
Zhao, X., Heslop, D., Roberts, A.P., 2015. A protocol for variable-resolution first-order reversal curve measurements. Geochem. Geophys. Geosyst. 16, 1364–1377.
Zheng, H.B., Powell, C.M., An, Z.S., Zhou, J., Dong, G.R., 2000. Pliocene uplift of the northern Tibetan Plateau. Geology 28, 715–718.
Zijderveld, J.D.A., 1967. AC demagnetization of rocks: analysis of results. In: Collinson, D.W., Creer, K.M., Runcorn, S.K. (Eds.), Methods in Paleomagnetism. Elsevier, New York, pp. 254–286.